

The University of Akron

IdeaExchange@UAkron

Williams Honors College, Honors Research
Projects

The Dr. Gary B. and Pamela S. Williams Honors
College

Summer 2022

Viscous Anisotropy of Wet Olivine Aggregates

Megan Ryan
mmr121@uakron.edu

Follow this and additional works at: https://ideaexchange.uakron.edu/honors_research_projects



Part of the [Geology Commons](#), [Geophysics and Seismology Commons](#), [Mineral Physics Commons](#), and the [Tectonics and Structure Commons](#)

Please take a moment to share how this work helps you [through this survey](#). Your feedback will be important as we plan further development of our repository.

Recommended Citation

Ryan, Megan, "Viscous Anisotropy of Wet Olivine Aggregates" (2022). *Williams Honors College, Honors Research Projects*. 1613.

https://ideaexchange.uakron.edu/honors_research_projects/1613

This Dissertation/Thesis is brought to you for free and open access by The Dr. Gary B. and Pamela S. Williams Honors College at IdeaExchange@UAkron, the institutional repository of The University of Akron in Akron, Ohio, USA. It has been accepted for inclusion in Williams Honors College, Honors Research Projects by an authorized administrator of IdeaExchange@UAkron. For more information, please contact mjon@uakron.edu, uapress@uakron.edu.

Viscous Anisotropy of Wet Olivine Aggregates

Megan Ryan

Advisor: Dr. Caleb Holyoke

Department of Geosciences

The University of Akron

August 10th, 2022

Abstract

Within the mantle wedge of subduction zones, seismic anisotropies are observed near the subducting slab as the fast seismic direction changes from trench perpendicular to trench parallel (Karato, 2003). Possible causes for this seismic anisotropy are trench parallel flow or a change in the dominant slip system in olivine crystals due to the presence of water which reorientates the fast seismic direction but does not change the flow direction. However, the exact cause is unclear. Results of deformation experiments on wet dunites by Jung et al. (2006) indicate the olivine Type C (slip in the c-direction along the a-plane; (100)[001]) and Type E (slip in the a-direction along the c-plane; (001)[100]) crystallographic preferred orientations (CPOs) should form at conditions of the mantle wedge, but these CPOs will not produce a fast seismic direction in the mantle wedge parallel to the trench. However, higher pressure deformation experiments on wet dunites by Ohuchi et. al. (2012) indicate Type B (slip in the c-direction on the b-plane) CPOs should form at conditions of the mantle wedge and this CPO puts the seismic fast direction parallel to the trench. In order to bridge the gap between these differing results, I performed experiments on a naturally deformed olivine aggregate with a pre-existing CPO. Cores for experiments were collected in three orientations relative to the CPO that put the slip systems that form the Type A, Type B, or Type C/E CPOs in easy slip orientations. Cores were deformed in the deformation-DIA multi-anvil press with a talc sleeve inside the assembly which dehydrated to hydrate the olivine. Results indicate that cores with the Type A (slip in the a-direction on the b-plane; (010)[100]) slip system orientation are slightly weaker than Type C/E cores and much weaker than Type B cores at low pressure ($P=1.11-1.18$ GPa) and low water contents ($\sim 700-1200$ H/ 10^6 Si). At intermediate pressures ($P=2-2.19$ GPa), the Type C/E cores are weaker than the Type B cores and much weaker than the Type A cores. At higher pressures ($P=2.58-3.13$ GPa), the Type B cores are weaker than both the Type A and Type C/E cores. These low

pressure results are consistent with those of Jung et al. (2006), but at higher pressures (and higher water contents) the Type B olivine CPO may become dominant, which is consistent with Ohuchi et. al. (2012). These results indicate that the dominant slip system in operation may change multiple times as it is hydrated during convection in the mantle wedge.

Introduction

Subduction zones are regions of convergence where one tectonic plate sinks into Earth's upper mantle, while a second tectonic plate rides above the sinking plate due to convection of Earth's upper mantle, which is driven by heat loss from Earth's core. These areas are prone to earthquakes and volcanic activity, as seen in the Cascadia subduction zone in the Western United States (Zhao and Hua, 2021). Seismologists use the fast direction of polarized seismic waves to infer the flow patterns of the mantle in subduction zones (Fischer et al., 1998; Mehl et al., 2003). Seismic polarization is caused by the alignment of the a-axes (100) of olivine grains in the mantle, which creates fast and slow wave propagation directions (Hess, 1964). A-axes become aligned because of deformation of olivine by dislocation creep, which usually involves slip of defects parallel to the a-axis on the b-plane of olivine crystals. In the mantle below the oceanic crust in large oceans, the fast direction is orientated parallel to the direction of plate motion, which is inferred to be parallel to the direction of mantle convective flow (Hess, 1964). In some subduction zones, mantle flow appears to change from trench perpendicular (parallel to the direction of subduction) to trench parallel (perpendicular to the direction of subduction) due to a change in the fast seismic polarization direction nearing the trench (Wiens and Smith, 2003; Karato, 2003; Ohuchi et al, 2012; Figure 1).

Possible causes of these seismic anisotropies are trench parallel flow of the mantle in the subduction zone (Fischer et al., 1998; Mehl et al., 2003; Conder and Wiens, 2007) or a change in the dominant olivine slip system due to the presence of water (Jung and Karato, 2001; Jung et al., 2006; Ohuchi et al., 2012). However, it is unlikely that trench parallel flow is the cause for observed seismic anisotropy within the upper mantle. The sudden change from trench perpendicular to trench parallel flow would require a complicated flow pattern. A change in the

dominant slip system of olivine due to hydration may be a simpler answer for the seismic anisotropies observed in subduction zones and does not require a flow pattern change within the upper mantle.

Water weakens olivine (Chopra and Paterson, 1984; Mackwell et al., 1985; Karato et al., 1986; Mei and Kohlstedt, 2000) and changes which slip system operates (Jung and Karato, 2001; Ohuchi et al., 2012). Likewise, subduction zones are hydrated by water released by serpentine dehydration in the subducting slab (Rüpke et al., 2004). Under hydrous conditions, olivine gains hydrogen point defects as hydrogen substitutes into olivine's crystal lattice, making it easier for dislocations to climb due to increased diffusion rates (Mei and Kohlstedt, 2000). Results of Jung et al. (2006; Figure 2) indicate the olivine Type C (slip in the c-direction along the a-plane; $(100)[001]$) and Type E (slip in the a-direction along the c-plane; $(001)[100]$) crystallographic preferred orientations should form at conditions of the mantle wedge (low stress, high water content), but these CPOs do not cause olivine $[100]$, the fast seismic direction to become aligned parallel to the trench in the mantle wedge like the CPO produced by Type B (slip in the c-direction on the b-plane). However, higher pressure experiments by Ohuchi et al. (2012) indicate only Type B CPO should form under mantle wedge conditions. Type A CPO (slip in the a-direction on the b-plane; $(010)[100]$) is observed in both natural rocks (Bernard et al., 2019), and experimentally-deformed rocks (Jung et al., 2006; Ohuchi et al., 2012), but only in olivine deformed at low stress and dry conditions, similar to the conditions of the oceanic lithosphere (Hirth and Kohlstedt, 2004).

In order to determine how increasing water content affects each of the slip systems in polycrystalline olivine and resolve the discrepancies between Jung et al. (2006) and Ohuchi et al. (2012), I deformed cores of olivine collected at three orientations relative to the crystallographic

preferred orientation (CPO) in a naturally deformed olivine aggregate (dunite) from Anita Bay, New Zealand (Chopra and Paterson, 1984; Figure 3). These cores were deformed in the presence of water at conditions that cause the aggregate to deform by dislocation creep. Cores of different orientations should have different viscosities and the weakest orientation should be the dominant slip system in hydrous olivine aggregates.

Methods

Sample Preparation

Cores of a fine-grained (average $d \cong 45 \mu\text{m}$) olivine aggregate from Anita Bay, New Zealand were used in all experiments (Chopra and Paterson, 1984). Visual microscopy of the starting material was done to determine grain size using the Zeiss Axioscope.AI petrographic microscope. The grain size of the undeformed Anita Bay dunite is $35 \pm 10 \mu\text{m}$ and $55 \pm 10 \mu\text{m}$ in fine-grained and coarse-grained regions of the starting material, respectively (Figure 4). The CPO of the starting material was determined using electron-backscattered diffraction (EBSD) in a scanning electron microscope (SEM). This technique maps the orientation of minerals and plots those data in both map and lower hemisphere stereo plots, which are used to determine if a CPO exists in the sample. EBSD analyses determined the undeformed Anita Bay dunite has a Type E CPO, which indicates the dunite previously deformed on the (001)[100] slip system (Figure 5). Dunite cylinders were cored in three orientations relative to the CPO in the Anita Bay dunite that put the slip systems that form the Type A, B or C/E CPOs in easy slip orientations (Figure 6). The 1.5 mm diameter cylinders were then ground perpendicular to the ends prior to each experiment.

Assembly Preparation

The sample assembly consists of a 9 mm pyrophyllite cube with two stacked dunite samples with differing CPOs surrounded by concentric talc, graphite, and alumina cylinders in a pyrophyllite cube (Figure 7). The talc cylinder dehydrate, forming orthopyroxene, quartz, and water, creating a hydrous environment around the dunite cylinders. The quartz adjacent to the dunite cylinders reacts with the olivine to form fine-grained orthopyroxene (Girard et al., 2013; Figure 8). Crushable alumina pistons are placed above and below the dunite cylinders in the load column and a thin disc of crushable alumina is placed in between the dunite cylinders. These crushable alumina cylinders deform during pressurization to minimize deformation of the dense dunite cylinders. Rhenium and nickel discs are placed at both ends of each dunite cylinder to act as x-ray absorbent markers (Re) and control oxygen fugacity (Ni).

Experimental Approach

Experiments were performed using the deformation-DIA multi-anvil press (D-DIA) located at beamline 6-BMB at the Advanced Photon Source at Argonne National Laboratory. The D-DIA is a cubic multi-anvil press with independently advancing load rams that axially deform the cylinders. Triaxial deformation of stacked olivine cylinders with differing CPOs allows me to determine relative viscosities of the dunite cylinders due to the differences in strain rates at identical deformational conditions (temperature, pressure, and stress). Synchrotron x-rays enter the press and diffract on suitably oriented grains (Figure 9). A semicircular ray of detectors and imaging plate gather both x-ray spectra and x-radiographs, respectively, during experiments.

Strain Rate and Stress Measurements

X-radiographs and x-ray spectra are collected during deformation and are used to determine strain rates and stress, respectively. The strain rates of each sample are determined by measuring displacements of x-ray absorbent Re foils at the ends of each dunite cylinder on x-radiographs using Image J (Figure 10). Strain measurements taken during deformation are time-correlated to provide strain rates (Figure 11). The x-ray spectra are collected from small regions (~100 micron x 100 micron x 1 mm) of alumina (top and bottom pistons, middle crushable alumina) near boundaries with olivine samples (Figure 12). X-ray spectra are collected and lattice plane peak positions within these spectra are determined using Plot85, a program used to analyze x-ray spectra data collected at Advanced Photon Source. Lattice plane spacing are determined using Bragg's Law;

$$n\lambda=2d\sin\theta \quad (\text{Eq. 1})$$

where n is the order of diffraction, λ is the wavelength, d is the crystal lattice spacing, and θ is the angle between the incident x-rays and the surface of the crystal. The changes in lattice plane spacing are determined by comparing the lattice plane spacing at room temperature and pressure to those measured at experimental conditions. These changes in lattice plane spacing are converted into pressure and differential stresses using Hooke's Law;

$$Fs = -kx \quad (\text{Eq. 2})$$

and assuming all deformation of the alumina pistons is elastic. Fs is the force applied to the pistons, k is the spring constant for the pistons, and x is amount of extension in the crystal.

Fourier-Transform Infrared Spectroscopy Measurements

Deformed samples are cut and polished parallel to the compression direction and perpendicular to the plane of dominant slip system using progressively-finer alumina grits. Once

polished on one side, sample halves are mounted to glass using dental wax and the other side is ground and polished to 94-217 μm thick. Samples are removed from the glass by heating the dental wax and soaking in acetone for a minimum of 5 minutes to dissolve any remaining wax. The water content of each dunite cylinder is determined from these sections utilizing Fourier-Transform Infrared Spectroscopy (FTIR). Water concentrations can be determined from the absorption of light in the wavelengths that correlate to water bond vibrations in olivine (3000-3650 cm^{-1}). I used the Paterson (1982) method to convert this absorbance into the amount of water within each dunite (Figure 13).

Results

Mechanical Data

I deformed stacked cylinders of Anita Bay dunite at $T=1200^\circ\text{C}$, $P=1.11\text{-}3.13$ GPa, and strain rates of 0.4×10^{-5} to 1.8×10^{-5} s^{-1} (Table 1). The strain rate increased with increasing pressure. At low pressures ($P=1.11\text{-}1.18$ GPa), the Type A core had the fastest strain rate (1.3×10^{-5} – 1.8×10^{-5} s^{-1}), the Type C/E core had an intermediate strain rate (1.1×10^{-5} s^{-1}) and the Type B core had the slowest strain rate (0.8×10^{-5} s^{-1}). At intermediate pressures ($P=2\text{-}2.19$ GPa), the Type C/E core had the fastest strain rate (1.7×10^{-5} s^{-1}), the Type B core had an intermediate strain rate (0.9×10^{-5} s^{-1}), and the Type A core had the slowest strain rate (0.6×10^{-5} s^{-1}). At $P=2.58$ GPa, both the Type B and the Type C/E core had a strain rate of 0.6×10^{-5} s^{-1} . At high pressures ($P=2.91\text{-}3.13$), the Type B core had the fastest strain rate (1.2×10^{-5} s^{-1}), the Type A core had an intermediate strain rate (0.4×10^{-5} – 0.5×10^{-5} s^{-1}), and the Type C/E core had the slowest strain rate (0.4×10^{-5} s^{-1}).

Differential stress remained low for each experiment. At low pressures (P=1.11-1.18 GPa), the differential stress was 170-220 MPa (Figure 14). At intermediate pressures (P=2-2.19 GPa), the differential stress was 20-150 MPa. At high pressures (P=2.58-3.13 GPa), the differential stress was 20-110 MPa.

The water contents of the cores were consistent with that of hydrated olivine and increased with increasing pressure. At low pressures (P=1.11-1.18 GPa), the dunite cores had low water contents ($\sim 700\text{-}1200 \text{ H}/10^6 \text{ Si}$). At intermediate pressures (P=2-2.19 GPa), the dunite cores had intermediate water contents ($\sim 1200\text{-}2100 \text{ H}/10^6 \text{ Si}$). At high pressures (P=2.58-3.13 GPa), the dunite cores had high water contents ($>\sim 2100 \text{ H}/10^6 \text{ Si}$).

Microstructural Data

Microstructures observed in the dunite cores from these experiments include flattened grains, undulatory extinction, and subgrain formation (Figure 15). No evidence for dynamic recrystallization was observed.

Discussion

I deformed stacked cores of Anita Bay dunite at $T=1200^\circ\text{C}$, $P=1.11\text{-}3.13 \text{ GPa}$, and strain rates of 0.4×10^{-5} to $1.8\times 10^{-5} \text{ s}^{-1}$. Strengths decreased as a function of increasing pressure and water content. Microstructures were similar in all samples and included flattened grains, undulatory extinction, and subgrain formation, which is consistent with microstructures formed by the deformation of wet olivine by dislocation creep in previous experimental studies (Jung et al., 2006; Ohuchi et al., 2012). Type A cores were weakest (fastest strain rate and lowest viscosity) at lower pressures (P=1.1-1.18 GPa; Figure 16), whereas Type C/E and Type B cores

were intermediate and strongest, respectively. These low pressure results are consistent with the of Jung et al. (2006). Type C/E and Type B cores were isoviscous at intermediate pressures (P=2-2.19 GPa). Type B cores were weakest (fastest strain rate and lowest viscosity) at higher pressures (>2.58 GPa), whereas Type A and Type C/E were intermediate and strongest, respectively. These high pressure results are consistent with the results of Ohuchi et al. (2012).

The results of my experiments and those of Jung et al. (2006) and Ohuchi et al. (2012) indicate that in the mantle wedge, the CPOs of dunite are expected to transition from Type A to Type B nearing the trench as water is released from the subducting plate beneath the mantle wedge. The intermediate range between Type A and in which Type C/E is dominant is a relatively small region of the upper mantle and may not be significant enough to be able detected seismically, but both Type C and E CPOs are observed in natural rocks (i.e., Bernard et al., 2019). Wang et al. (2022) deformed olivine single crystals in order to activate a- and c- dislocations. Once annealed, annihilation rates of a- and c-dislocations were measured, which shows the effect of water on dislocation mobility. They found that both Type A and Type C have similar values for the water content exponent of the annihilation coefficient. These results imply that there is not a significant viscosity difference between Type A and Type C. However, Wang et al. (2022) did not determine the annihilation coefficient for dislocations produced by the slip system that forms the Type B CPO. My results are consistent with those of Wang et al. (2022) in that the viscosity change between Type A and Type C is not significant. However, my results also indicate that water has a significant effect on the viscosity of the slip system which forms the Type B CPO.

The log viscosity of the CPOs decreases with increasing pressure (Figure 17). At low pressures (< ~1.7 GPa), Type A has the lowest viscosity, Type C/E has an intermediate viscosity,

and Type B has the highest viscosity. Lower viscosities correlate to higher strain rates and weaker orientations. At intermediate pressures (~1.7-2 GPa), Type C/E has the lowest viscosity, Type B has an intermediate viscosity, and Type A has the highest viscosity. At high pressures (>2 GPa), Type B has the lowest viscosity, whereas Type A and C/E have similar viscosities. The viscosities of the CPOs evolve with increasing pressure and water content. Type B has the lowest viscosity at the highest pressure and water contents, which is consistent with the changes necessary to produce a trench parallel seismic anisotropy.

With increasing pressure and water content, the viscous anisotropy of the Anita Bay dunite cores does not change significantly despite changes in the dominant slip system (Figure 18). These viscous anisotropy values show a consistent trend with the low-pressure, dry experiments of Hansen et al. (2012). They conducted both torsion and tension tests on olivine aggregates to determine the viscous anisotropy at $P=300$ MPa and dry conditions. These results indicate that the addition of water does not reduce the viscous anisotropy in olivine aggregates and the viscous anisotropy of dunites will remain high in the hydrated mantle wedge. However, the weak slip system will change from Type A to Type B as the upper mantle is hydrated, which puts the fast seismic direction in a trench parallel configuration. This new orientation puts strong slip systems parallel to the trench, which will limit flow perpendicular to plate motion.

Conclusion

I deformed a natural polycrystalline olivine aggregate to determine how different slip systems are affected by increasing water content. Within the mantle, water plays an important role in olivine deformation, as well as in the upper mantle seismic anisotropy seen in some

subduction zones. My results indicate that the slip system that produces the Type A CPO is weakest at low pressures and low water contents ($P=1.11-1.18$ GPa; $\sim 700-1200$ H/ 10^6 Si). At intermediate pressures ($P=2-2.58$ GPa; $\sim 1200-2100$ H/ 10^6 Si), the slip systems that produce the Type C and Type E CPOs are weakest. At high pressures ($P=2.91-3.13$ GPa; $>\sim 2100$ H/ 10^6 Si), the slip system that produces the Type B CPO becomes dominant. Moreover, my results have the following implications to nature:

- Hydrous olivine aggregates undergo two major transitions in the dominant slip system with increasing pressure and water content.
- The CPOs of olivine are expected to transition from Type A to B nearing the trench as water is released from the subducting plate beneath the wedge. The region where Type C/E becomes dominant may not be significant enough to detect seismically.
- Hydrous olivine aggregates also undergo a change in viscosity as different slip systems become dominant. Noticeably, there is a reduction in viscosity between the Type A to Type C/E transition.
- Both the change in slip system and viscosity are likely to play a role in the upper mantle seismic anisotropy seen in some subduction zones.

References

- Bernard, R.E., Behr, W.M., Becker, T.W., Young, D.J., 2019. Relationships between olivine CPO and deformation parameters in naturally deformed rocks and implications for mantle seismic anisotropy. *Geochemistry, Geophysics, Geosystems* 20, 3469-3494. <https://doi.org/10.1029/2019GC008289>.
- Conder, J.A., Wiens, D.A., 2007. Rapid mantle flow beneath the Tonga volcanic arc. *Earth and Planetary Science Letters* 264, 299-307. <https://doi.org/10.1016/j.epsl.2007.10.014>.
- Chopra, P.N., Paterson, M.S., 1984. The role of water in the formation of dunite. *Journal of Geophysical Research* 89, 7861-7876. [https://doi.org/10.1016/0040-1951\(81\)90024-X](https://doi.org/10.1016/0040-1951(81)90024-X).
- Fischer, K.M., Fouch, M.J., Wiens, D.A., Boettcher, M.S., 1998. Anisotropy and flow in Pacific subduction zone back-arcs. *Pure and Applied Geophysics* 151, 463-475. <https://doi.org/10.1007/s000240050123>.
- Girard, J., Chen, J., Ratteron, P., Holyoke, C., III, 2013. Hydrolytic weakening of olivine at mantle pressure: Evidence of [100](010) slip system softening from single-crystal deformation experiments. *Physics of the Earth and Planetary Interiors* 216, 12-20. <https://doi.org/10.1016/j.pepi.2012.10.009>.
- Hansen, L., Zimmerman, M., Kohlstedt, D., 2012. Laboratory measurements of the viscous anisotropy of olivine aggregates. *Nature* 492, 415-418. <https://doi.org/10.1038/nature11671>.
- Hess, H., 1964. Seismic anisotropy of the uppermost mantle under oceans. *Nature* 203, 629-631. <https://doi.org/10.1038/203629a0>.
- Hirth, G., Kohlstedt, D., 2004. Rheology of the upper mantle and the mantle wedge: a view from the experimentalists. *Inside the Subduction Factory*, Geophysical Monograph 138. <https://doi.org/10.1029/138GM06>.
- Jung, H., Karato, S., 2001. Water-induced fabric transitions in olivine. *Science* 293, 1460-1463. <https://doi.org/10.1126/science.1062235>.
- Jung, H., Katayama, I., Jiang, Z., Hiraga, T., Karato, S., 2006. Effect of water and stress on lattice-preferred orientation of olivine. *Tectonophysics* 421, 1-22. <https://doi.org/10.1016/j.tecto.2006.02.011>.
- Karato, S.-I., Paterson, M.S., FitzGerald, J.D., 1986. Rheology of synthetic olivine aggregates: influence of grain size and water. *Journal of Geophysical Research* 91, 8151-8176. <https://doi.org/10.1029/JB091iB08p08151>.
- Karato, S.-I., 2003. Mapping water content in the upper mantle. *Inside the Subduction Factory*, Geophysical Monograph 138. <https://doi.org/10.1029/138GM08>.

- Mackwell, S.J., Kohlstedt, D.L., Paterson, M.S., 1985. The role of water in the deformation of olivine single crystals. *Journal of Geophysical Research* 90, 11319-11333. <https://doi.org/10.1029/JB090iB13p11319>.
- Mehl, L., Hacker, B.R., Hirth, G., Keleman, P.B., 2003. Arc-parallel flow within the mantle wedge: Evidence from the accreted Talkeetna arc, south central Alaska. *Journal of Geophysical Research* 108, 2375. <https://doi.org/10.1029/2002JB002233>.
- Mei, S., Kohlstedt, D.L., 2000. Influence of water on plastic deformation of olivine aggregates 2. Dislocation creep regime. *Journal of Geophysical Research* 105, 21471-21481. <https://doi.org/10.1029/2000JB900180>.
- Ohuchi, T., Kawazoe, T., Nishihara, Y., Irifune, T., 2012. Change of olivine a-axis alignment induced by water: Origin of seismic anisotropy in subduction zones. *Earth and Planetary Science Letters* 317-318, 111-119. <https://doi.org/10.1016/j.epsl.2011.11.022>.
- Paterson, M.S., 1982. The determination of hydroxyl by infrared absorption into quartz, silicate glasses, and similar materials. *Bulletin de Minéralogie* 105, 20-29. <http://dx.doi.org/10.3406/bulmi.1982.7582>.
- Rüpke, L., Phipps Morgan, J., Hort, M., Connolly, J., 2004. Serpentine and the subduction zone water cycle. *Earth and Planetary Science Letters* 223, 17-34. <https://doi.org/10.1016/j.epsl.2004.04.018>.
- Wang, L., Chanyshv, A., Miyajima, N., Kawazoe, T., Blaha, S., Chang, J., Katsura, T., 2022. Small effect of water incorporation on dislocation mobility in olivine: Negative creep enhancement and water-induced fabric transition in the asthenosphere. *Earth and Planetary Science Letters* 579, 117360. <https://doi.org/10.1016/j.epsl.2021.117360>.
- Wiens, D.A., Smith, G.P., 2003. Seismological constraints on structure and flow patterns within the mantle wedge. *Inside the Subduction Factory*, Geophysical Monograph 138. <https://doi.org/10.1029/138GM05>.
- Zhao, D., Hua, Y., 2021. Anisotropic tomography of the Cascadia subduction zone. *Physics of the Earth and Planetary Interiors* 318, 2-20. <https://doi.org/10.1016/j.pepi.2021.106767>.

Table 1. Experimental conditions and results.

Experiment Number	Top or bottom?	CPO	Pressure, P (GPa)	Differential Stress, σ (MPa)	Strain Rate, $\dot{\epsilon}$ ($\times 10^{-5} \text{ s}^{-1}$)	Water Content (H/ 10^6 Si)
GM_037	Top	Type A	1.11	220	1.8	780
	Bottom	Type B			0.8	2570
GM_033	Top	Type A	1.18	170	1.3	1090*
	Bottom	Type C/E			1.1	1090*
GM_038	Top	Type A	2	60	0.6	1380
	Bottom	Type B			0.9	2090
GM_035	Top	Type A	2.19	150	0.6	1630
	Bottom	Type C/E			1.7	1600
GM_044	Top**	Type B	2.58	20	0.6	-
	Bottom	Type C/E			0.6	1580
GM_042	Top	Type A	2.91	40	0.4	3220
	Bottom	Type B			1.2	1550
GM_041	Top	Type A	3.13	110	0.5	1800
	Bottom	Type C/E			0.4	2040

* Sample damaged during preparation, orientation (top or bottom) of the FTIR spectra unknown.

** Sample damaged during preparation.

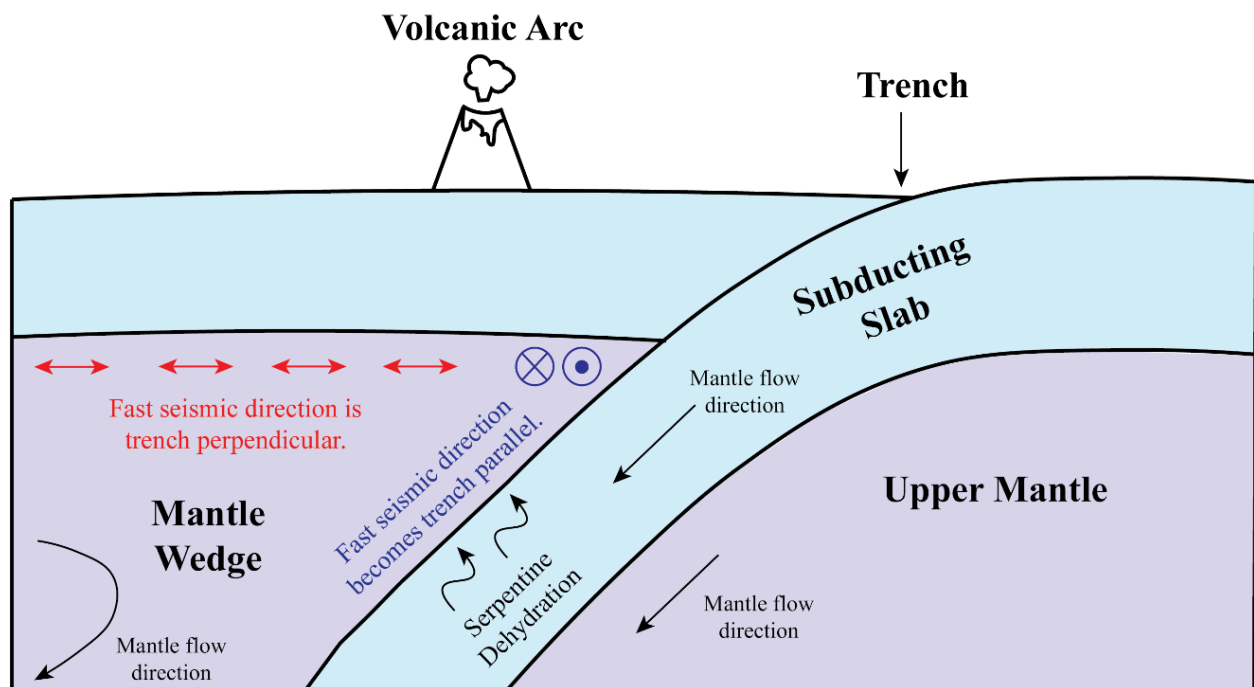


Figure 1. Illustration of a subduction zone with orientations of the fast seismic directions shown.

Diagram not to scale.

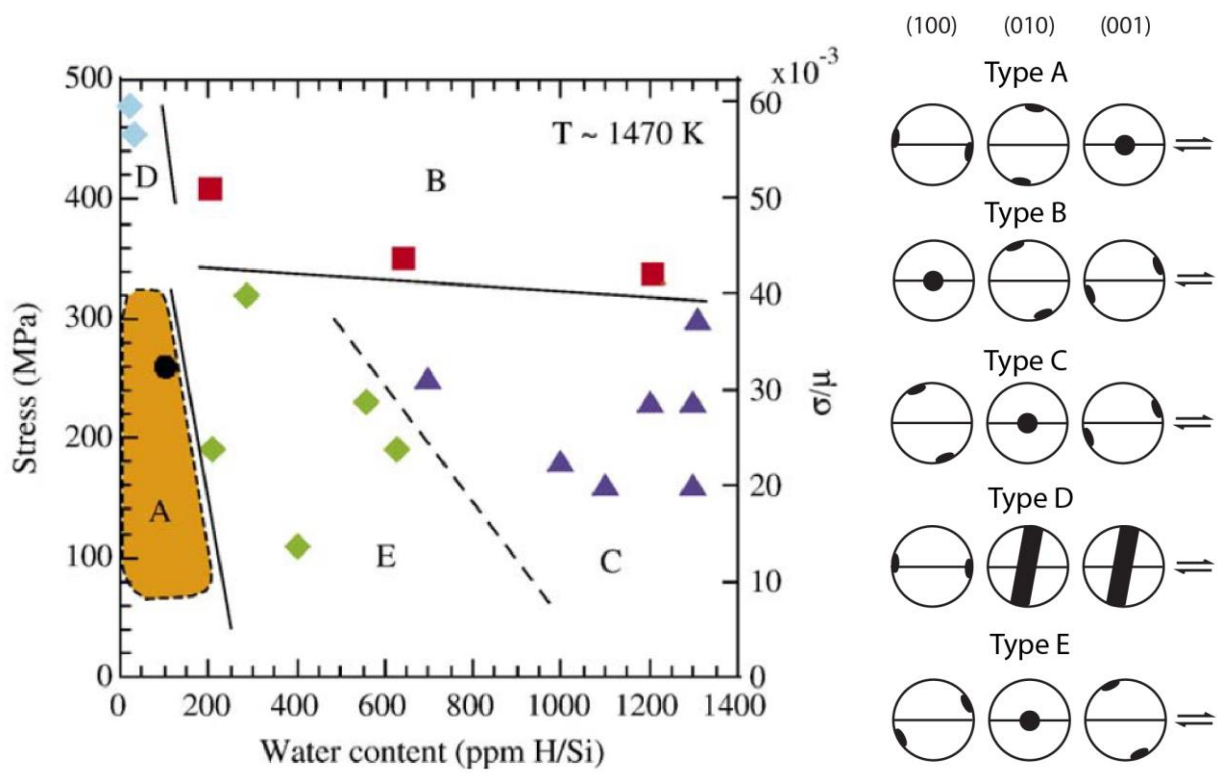


Figure 2. Fabric diagram showing the results of olivine deformation experiments by Jung et al. (2006) conducted at $T \sim 1470\text{--}1570$ K showing the dominant fabric as a function of stress and water content.

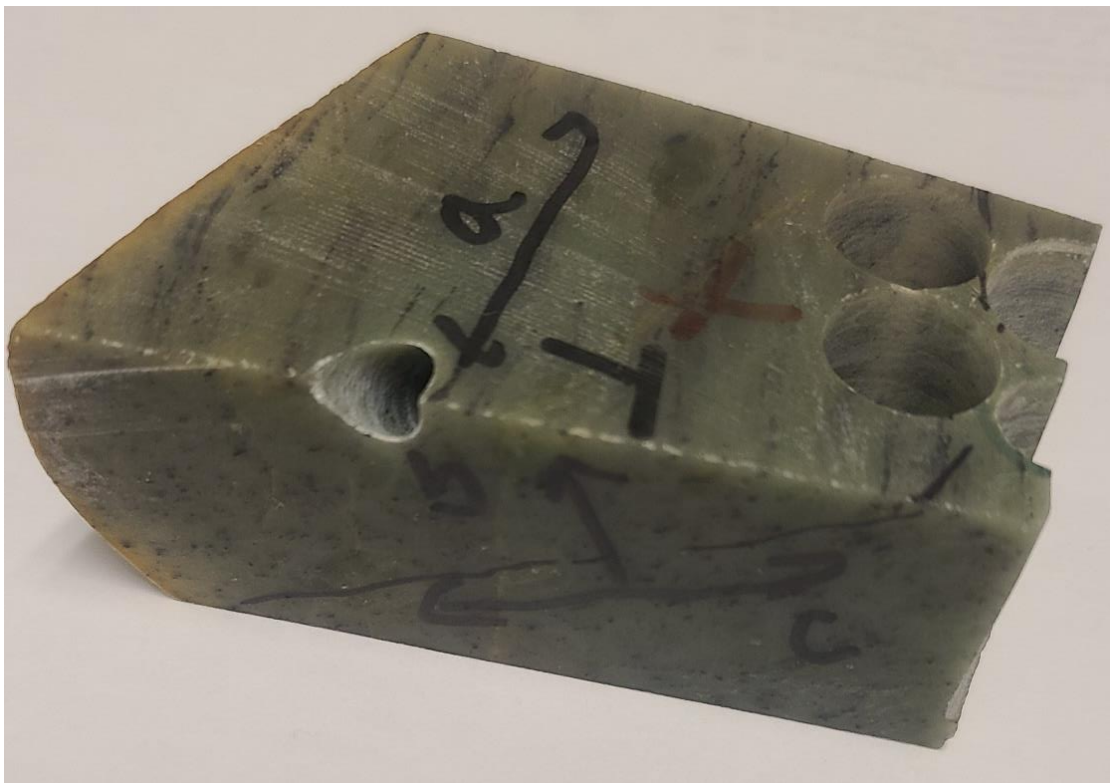


Figure 3. Photo of Anita Bay dunite sample with a, b, and c axes labeled (10 cm wide), foliation and lineation are defined by the elongate black chromite grains.

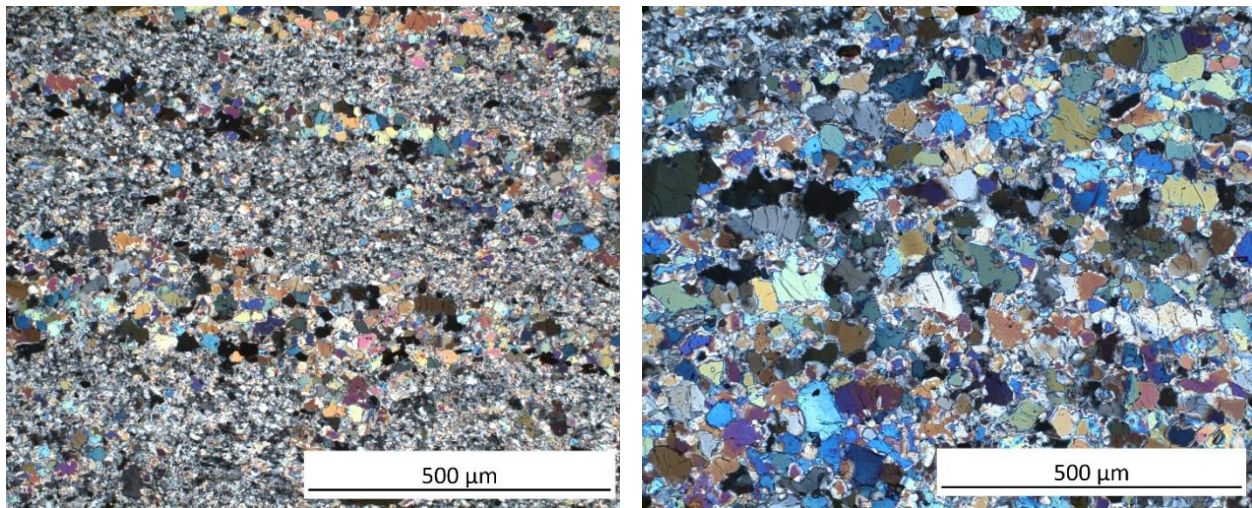


Figure 4. Cross-polarized optical images of Anita Bay dunite, with foliation orientation horizontal in both images. High interference colored grains indicate olivine, extinct grains indicate chromite grains.

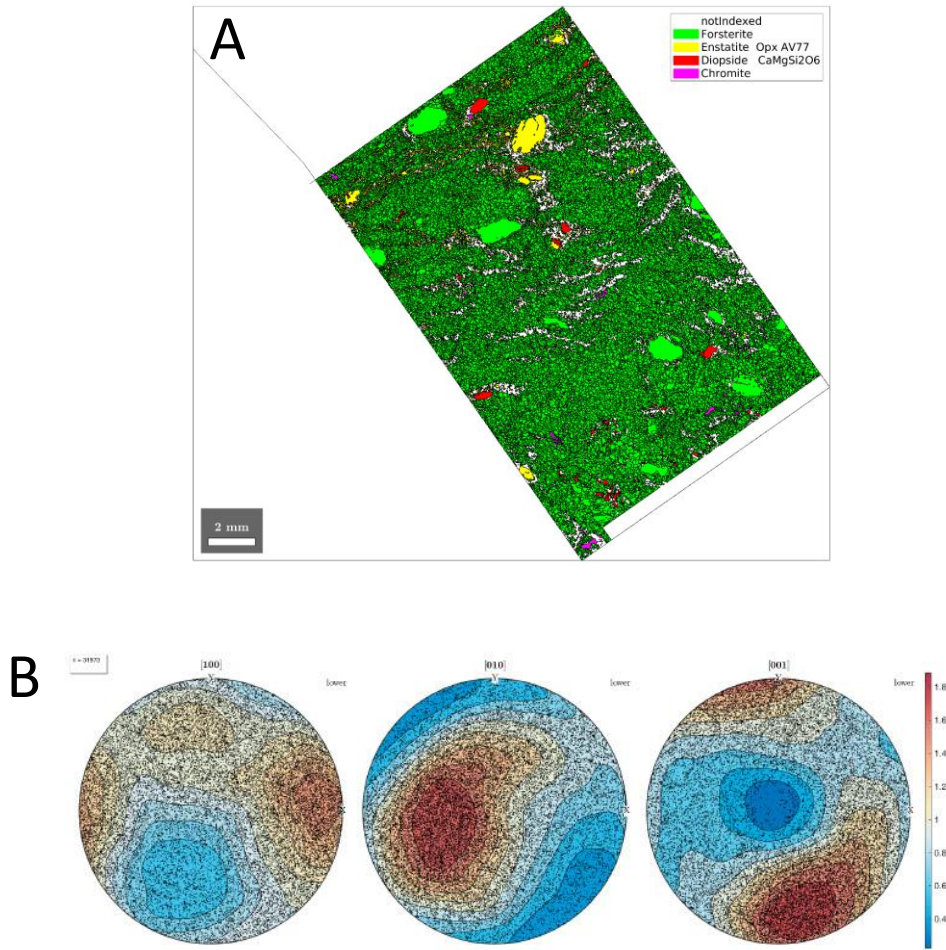


Figure 5. **A)** Phase map for Anita Bay dunite showing phases present (top). **B)** Lower hemisphere equal area projection of olivine crystallographic preferred orientation (CPO) measurements within the Anita Bay dunite, as well as the Type E CPO of the sample (bottom). Black dots indicate individual grain measurements.

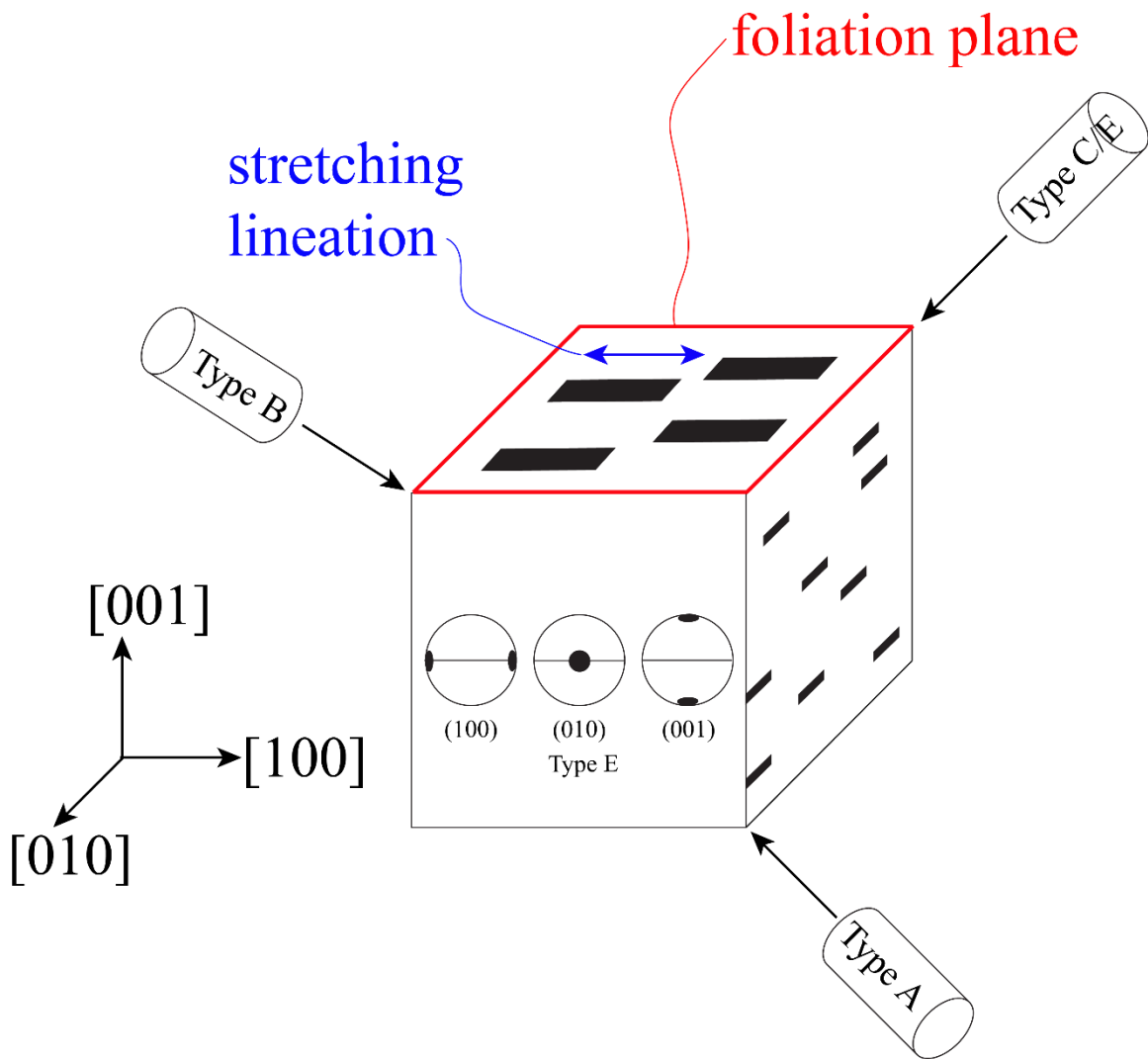


Figure 6. Core orientation diagram showing relation to the overall CPO of the starting Anita Bay dunite sample. Cores of Type A, B, and C/E were taken from the starting material.

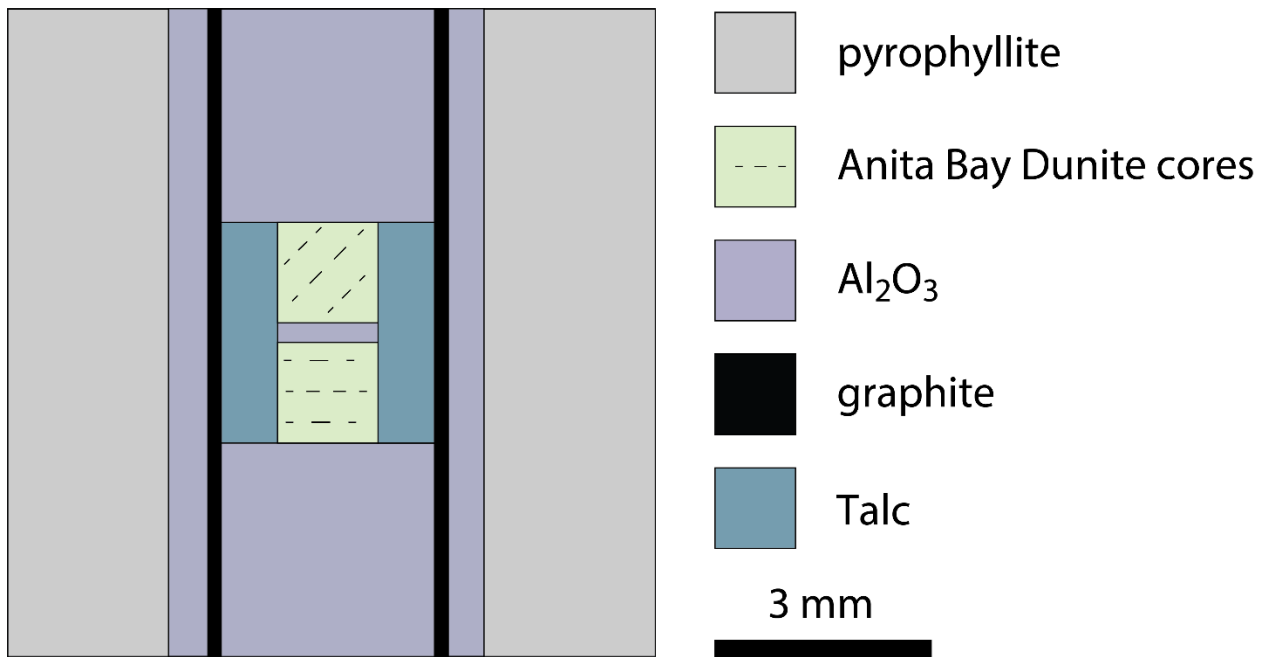


Figure 7. D-DIA assembly used in each deformation experiment conducted on the Anita Bay dunite in this study. Dashed lines indicated different CPO orientations of stacked dunite cores.

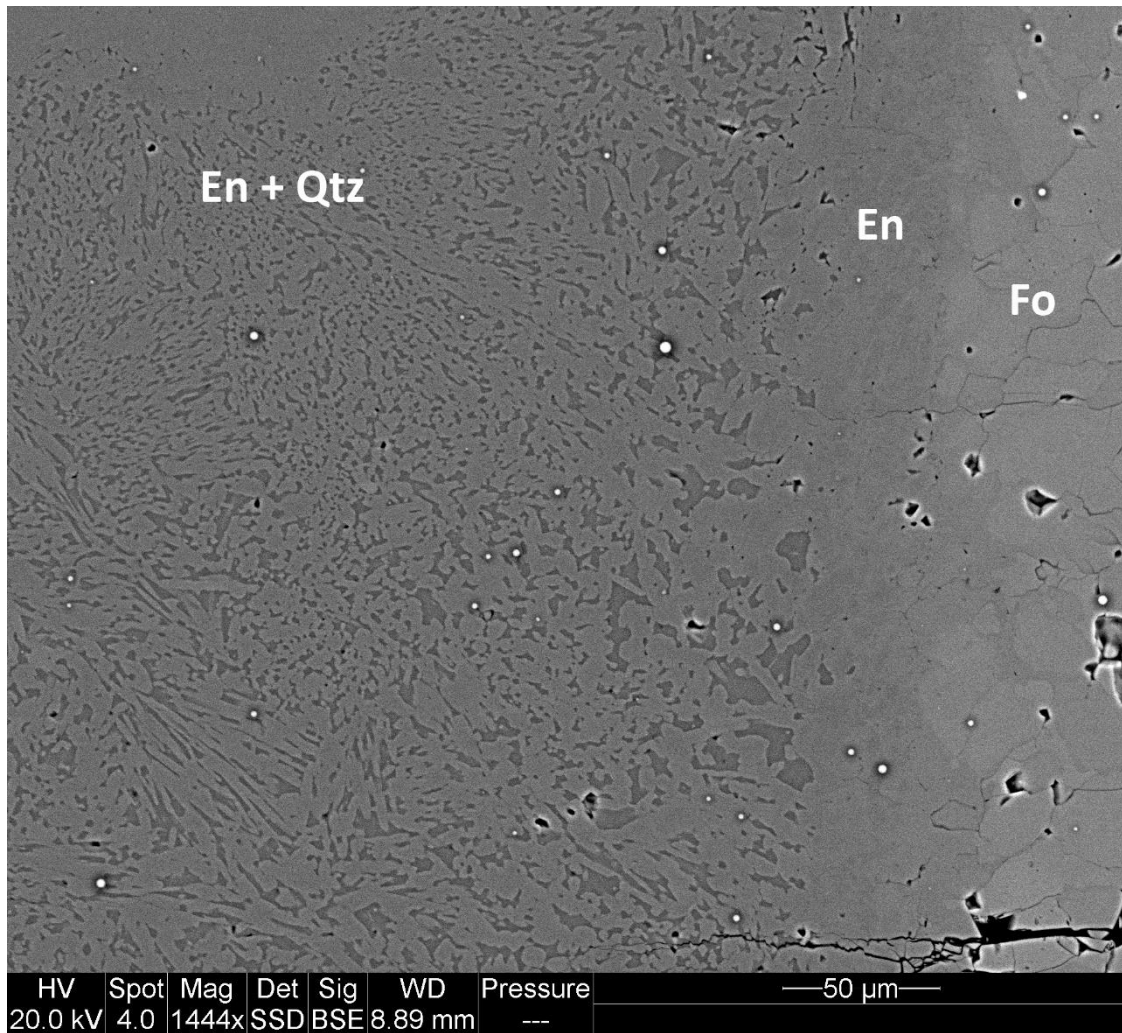


Figure 8. SEM image of the reaction rim (En) between polycrystalline olivine (Fo; right) and dehydrated talc sleeve (En + Qtz; left) in experiment GM_042. Horizontal cracks in the dunite are from unloading post-deformation.

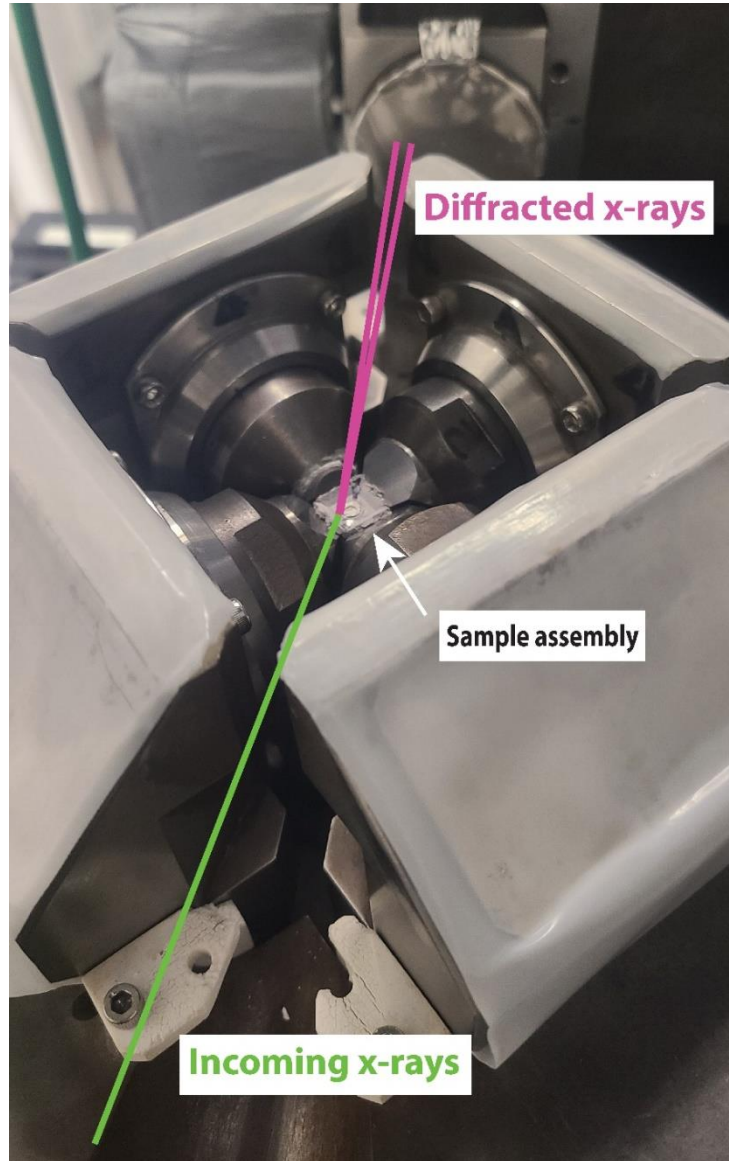


Figure 9. Photo showing the path of x-ray beams as they enter the press and diffract off of suitably orientated olivine lattice planes.

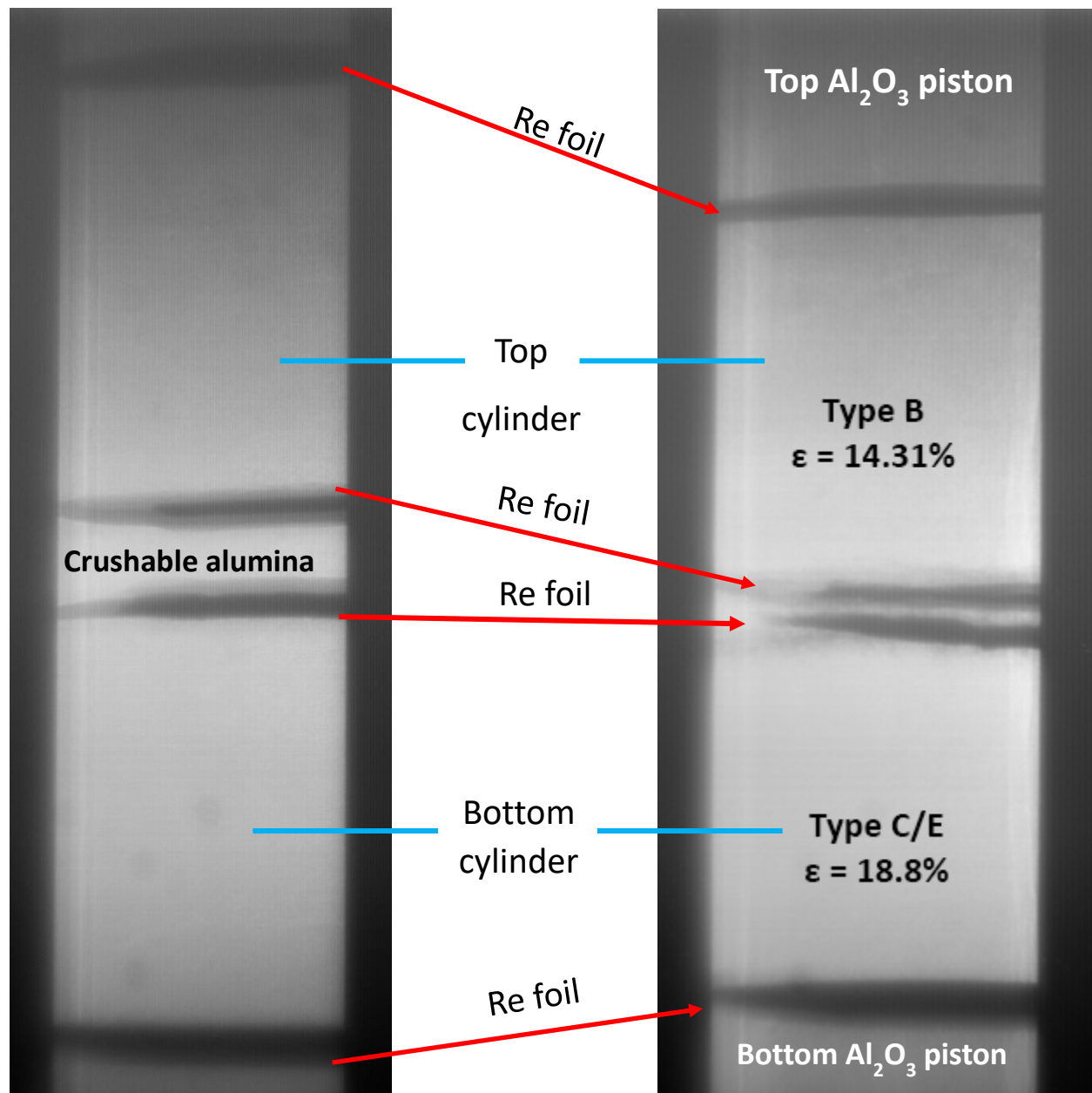


Figure 10. X-radiographs showing experiment GM_044 under undeformed (left) and deformed (right) conditions ($T=1200^{\circ}\text{C}$, $P=2.58\text{ GPa}$). The x-ray absorbency of Re foil allows the strain rates of the samples to be calculated.

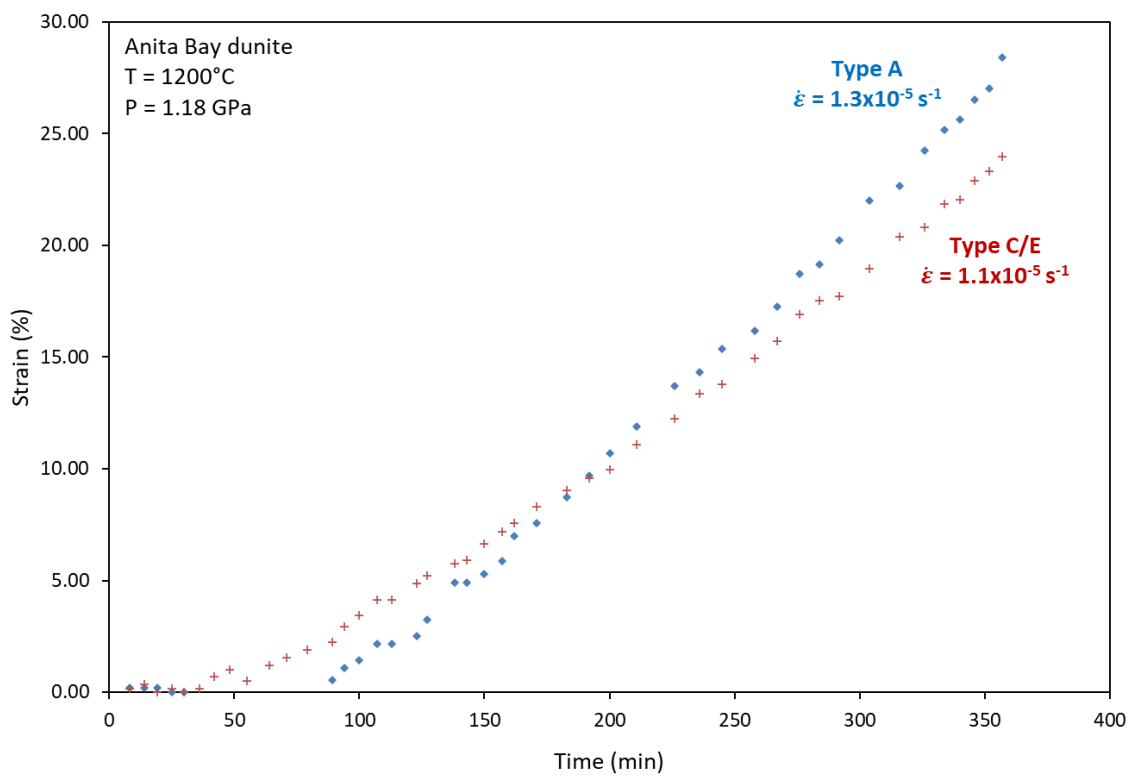


Figure 11. Strain (%) versus time (min) for experiment GM_033. The Type A core has a faster strain rate than the Type C/E core.

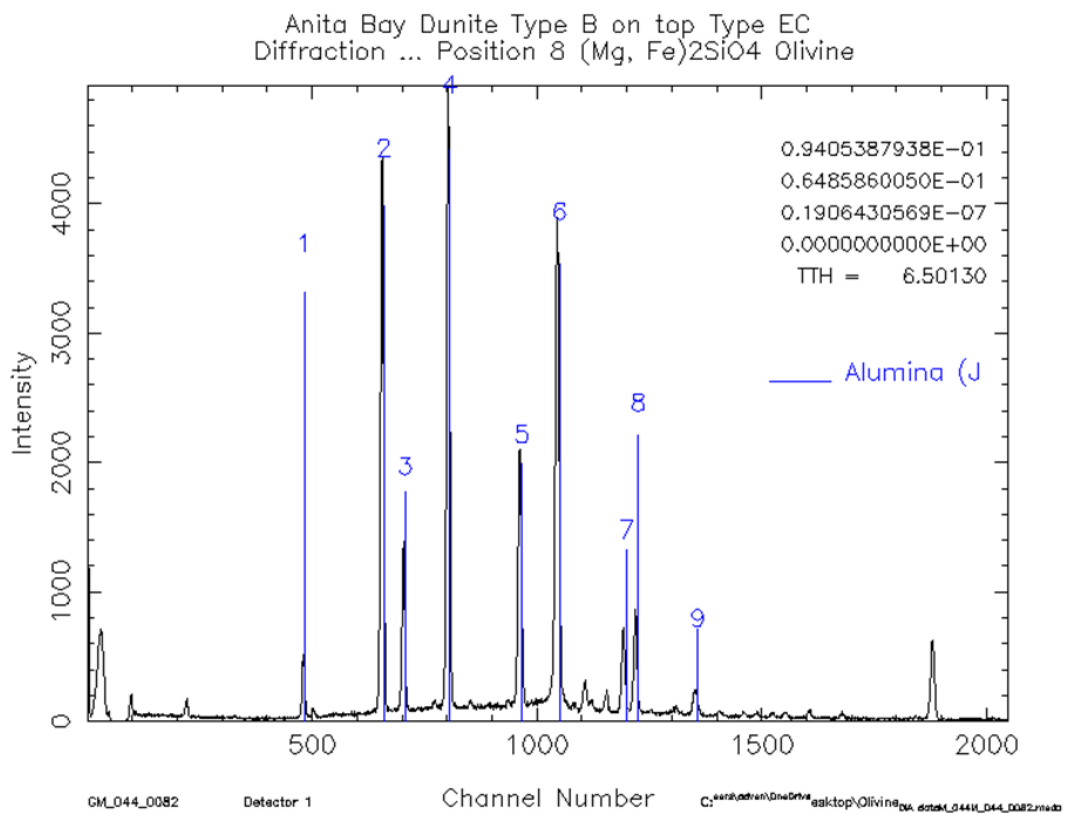


Figure 12. X-ray spectra showing the spectra collected from a region of crushable alumina during deformation. Peaks 2-6 were used to determine temperature and pressure ($T=1200^{\circ}\text{C}$, $P=2.58\text{ GPa}$). Locations for x-ray spectra collection cycle through top alumina piston, middle crushable alumina, and bottom alumina piston.

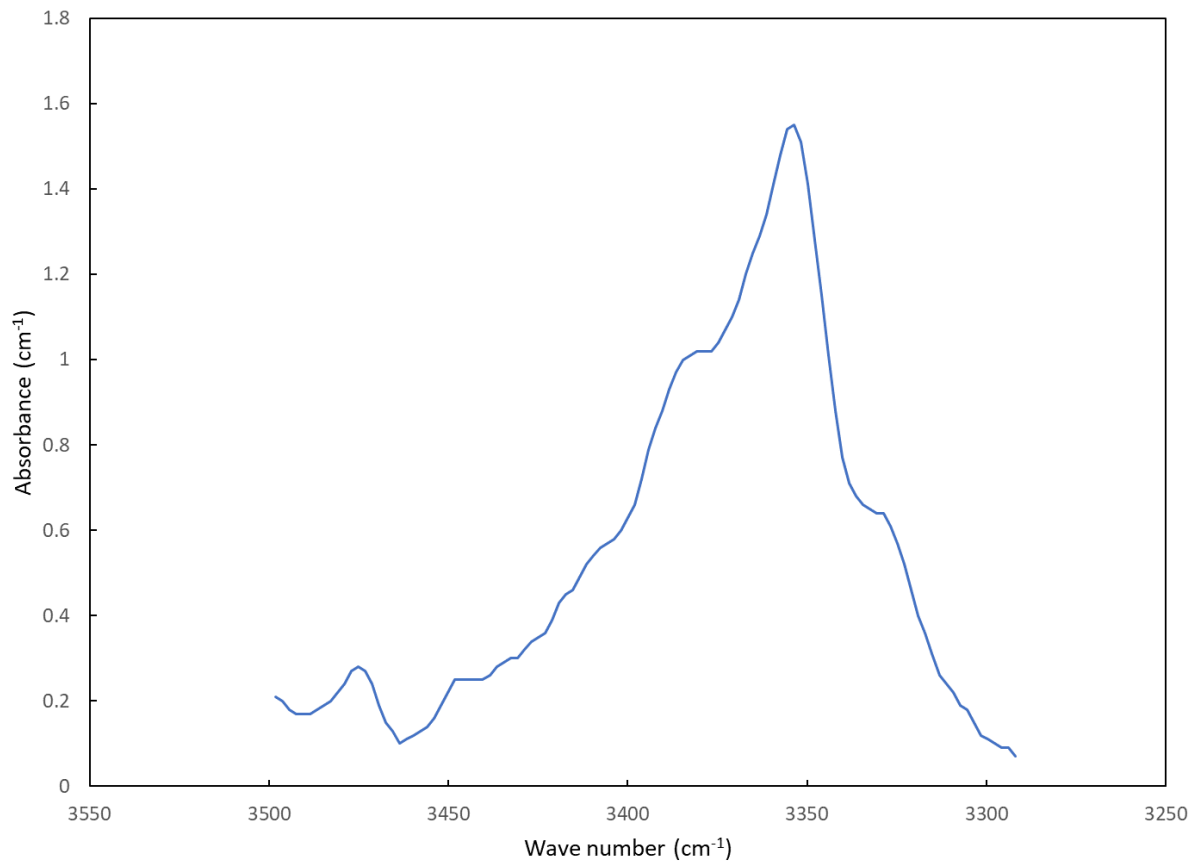


Figure 13. Fourier-transform infrared spectra collected from the top core (Type A) of GM_041, showing the absorbance due to OH⁻ point defects in the olivine.

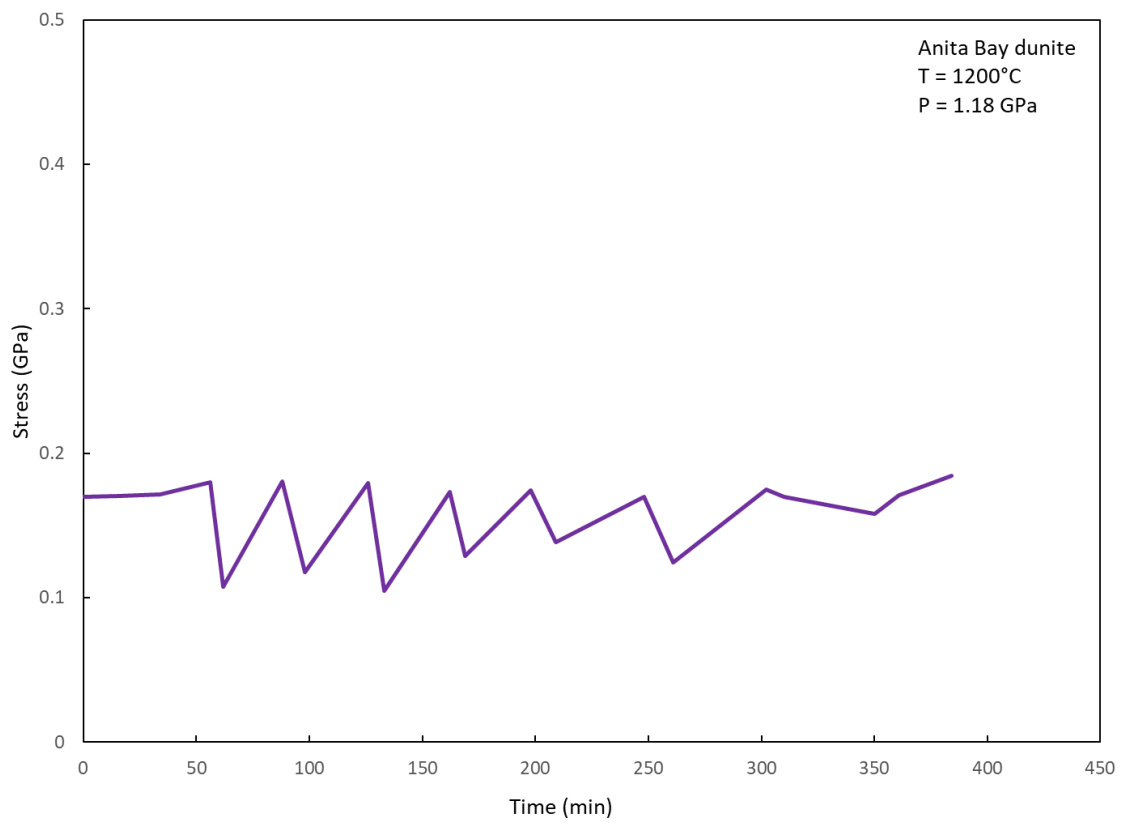


Figure 14. Differential stress graph for experiment GM_033, showing average stress (GPa) plotted against time (min).

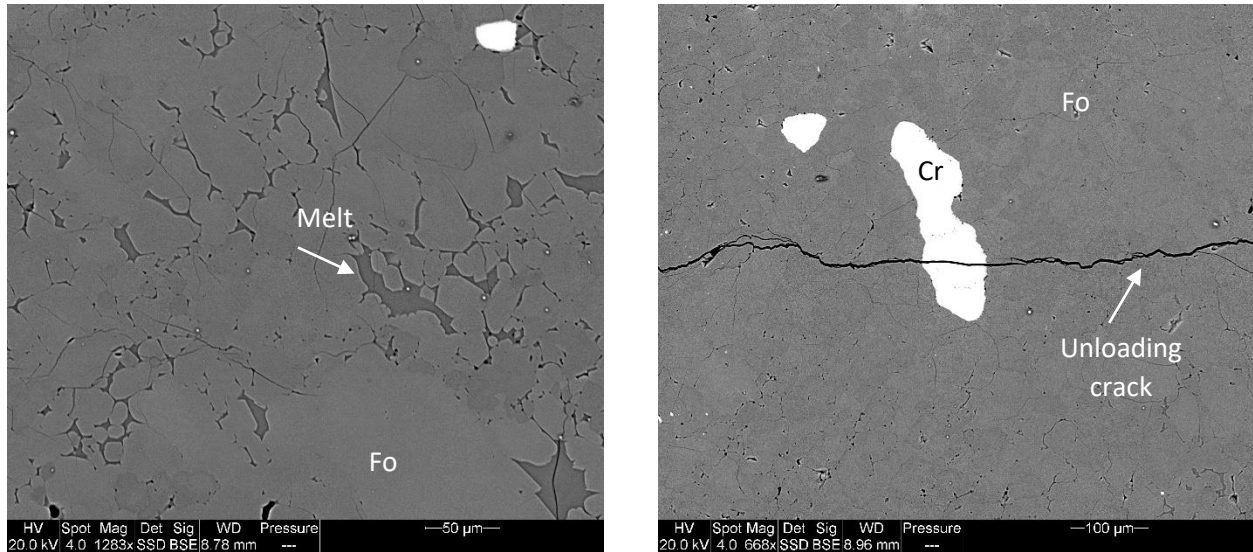


Figure 15. Scanning electron microscope images of experiment GM_037 (deformed at 1.5 GPa). Microstructures in the deformed samples are consistent with previous deformation studies and include minor flattening of grains, undulatory extinction, and subgrain formation (not pictured). **A)** Small amounts of melt (<1%) are seen above, but many regions remain melt-free. **B)** A chromite grain is crosscut by an unloading crack formed during depressurization of the samples post-deformation.

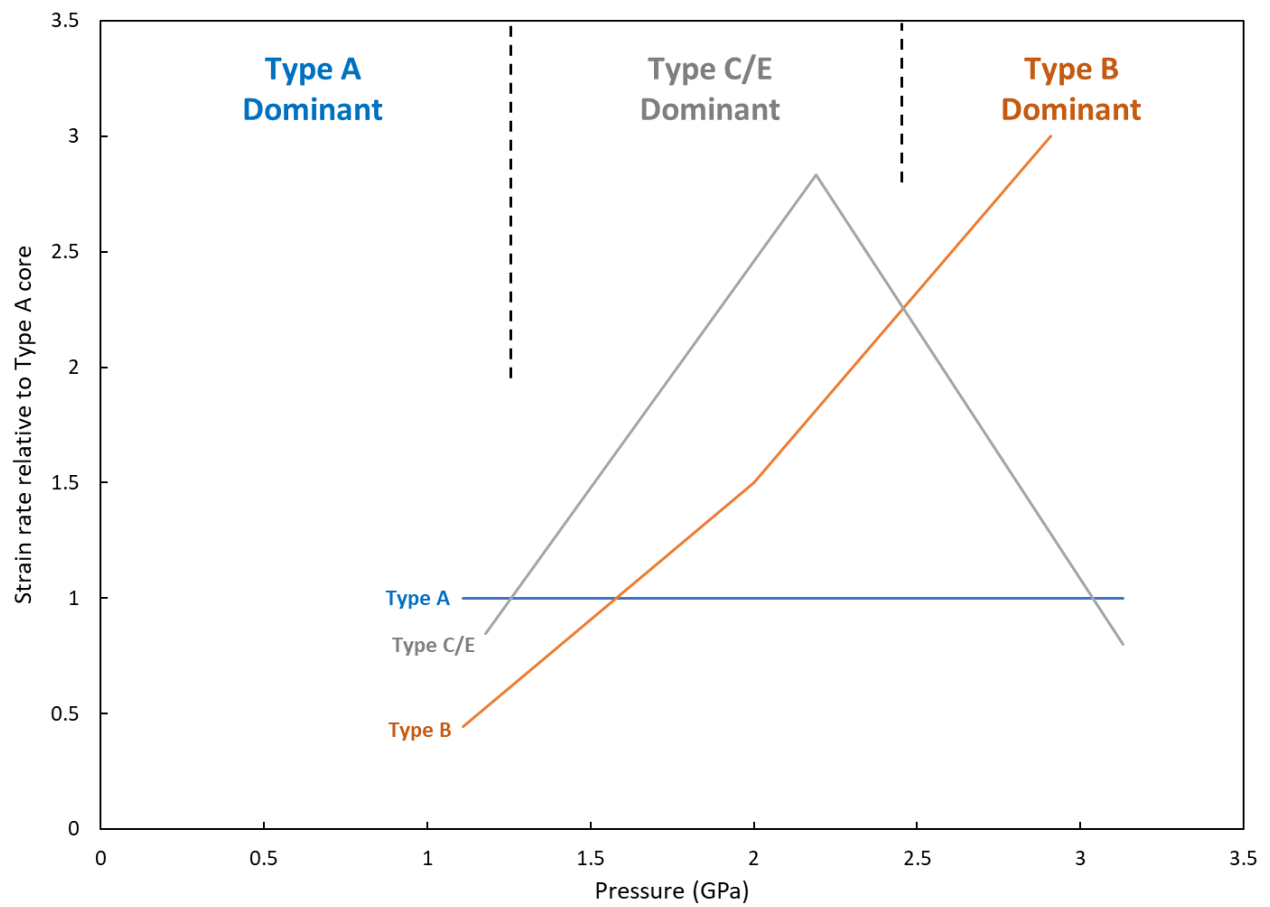


Figure 16. The relative strain rates of cores oriented for easy slip on different slip systems vary as a function of increasing pressure and water content.

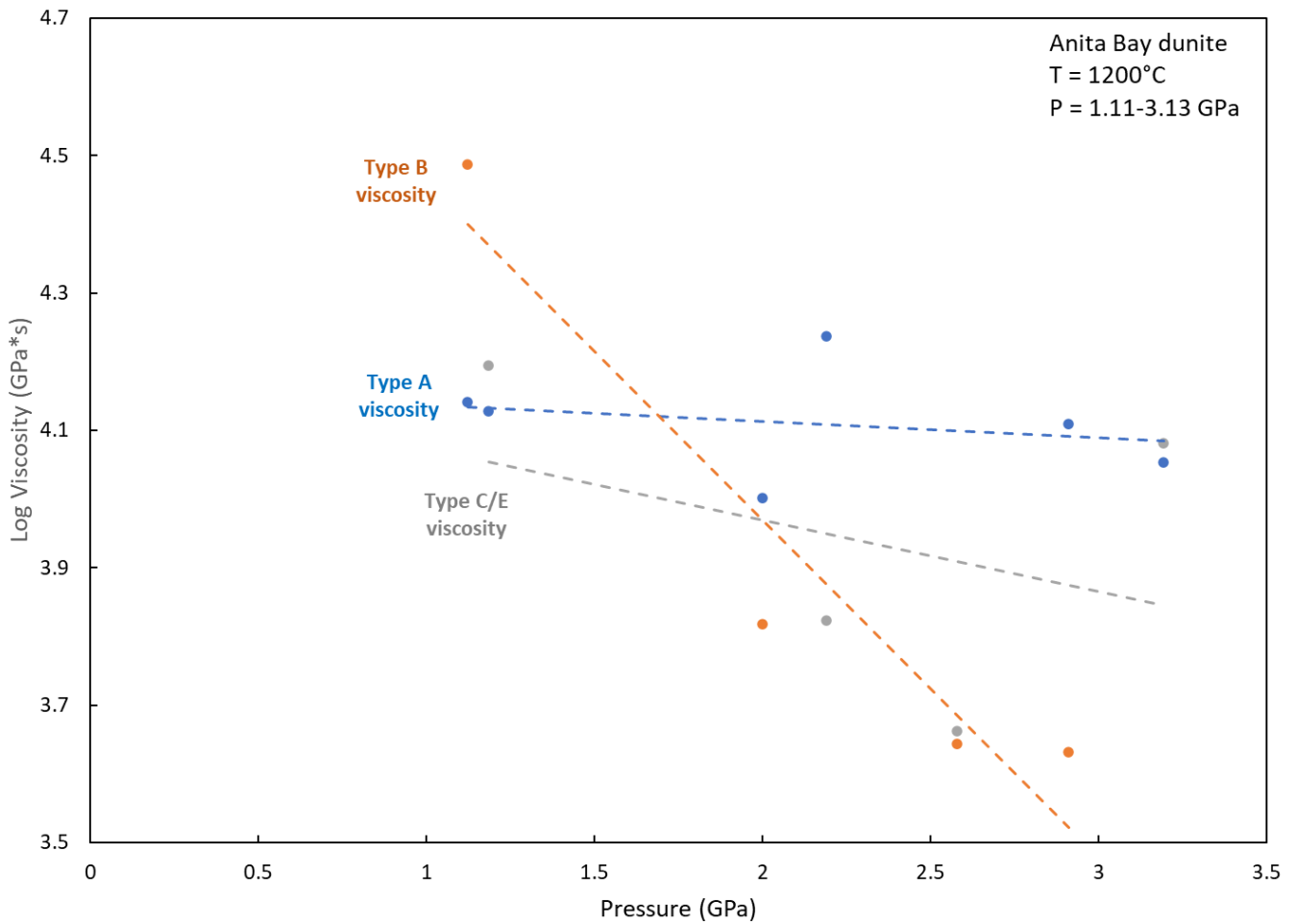


Figure 17. Log viscosity (GPa*s) versus pressure (GPa) for all deformation experiments in this study. Viscosity decreases as a function of increasing pressure and water content. Type A cores are weakest at low pressures, Type C/E cores are weakest at intermediate pressures, and Type B cores are weakest at high pressures.

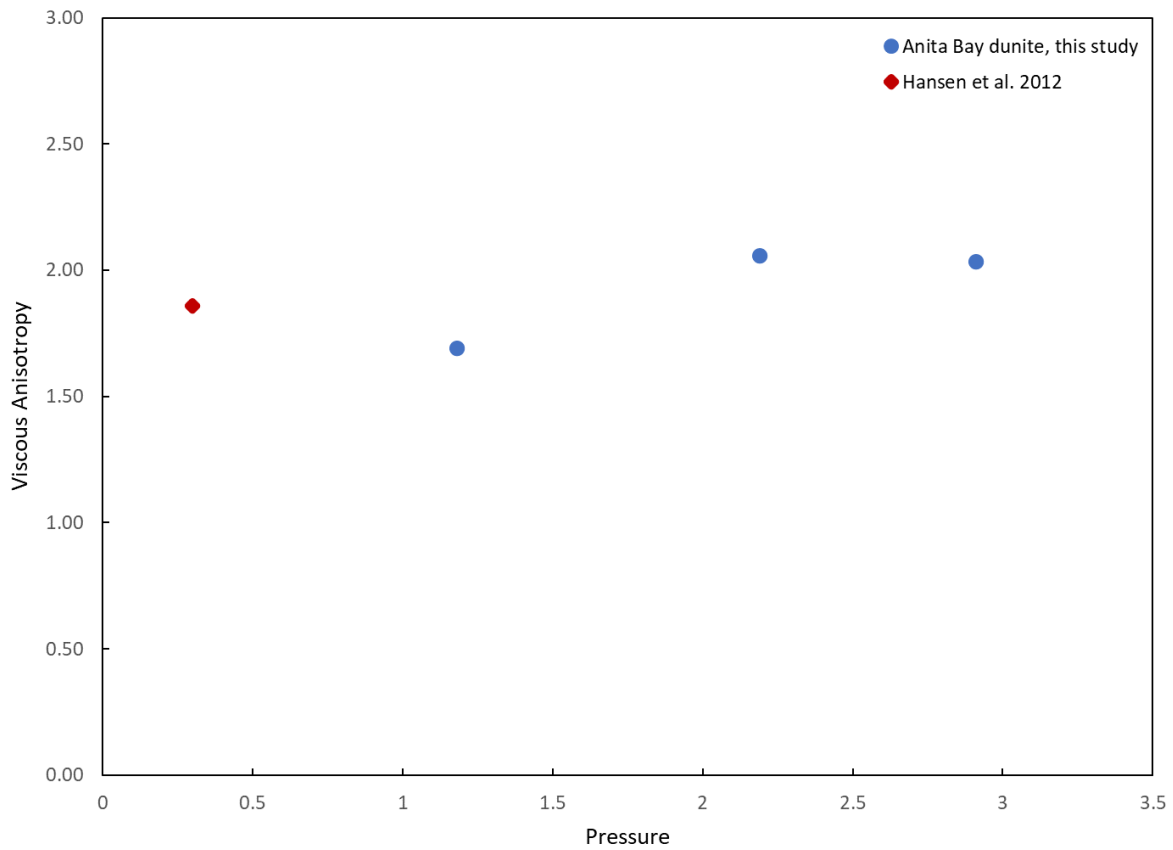


Figure 18. Viscous anisotropy versus pressure (GPa) for the deformed dunite samples from this study (blue). Viscous anisotropy increases with increasing pressure and water content during the development of a dominant CPO. The results of this study are consistent with those of Hansen et al. (2012) shown above (red).

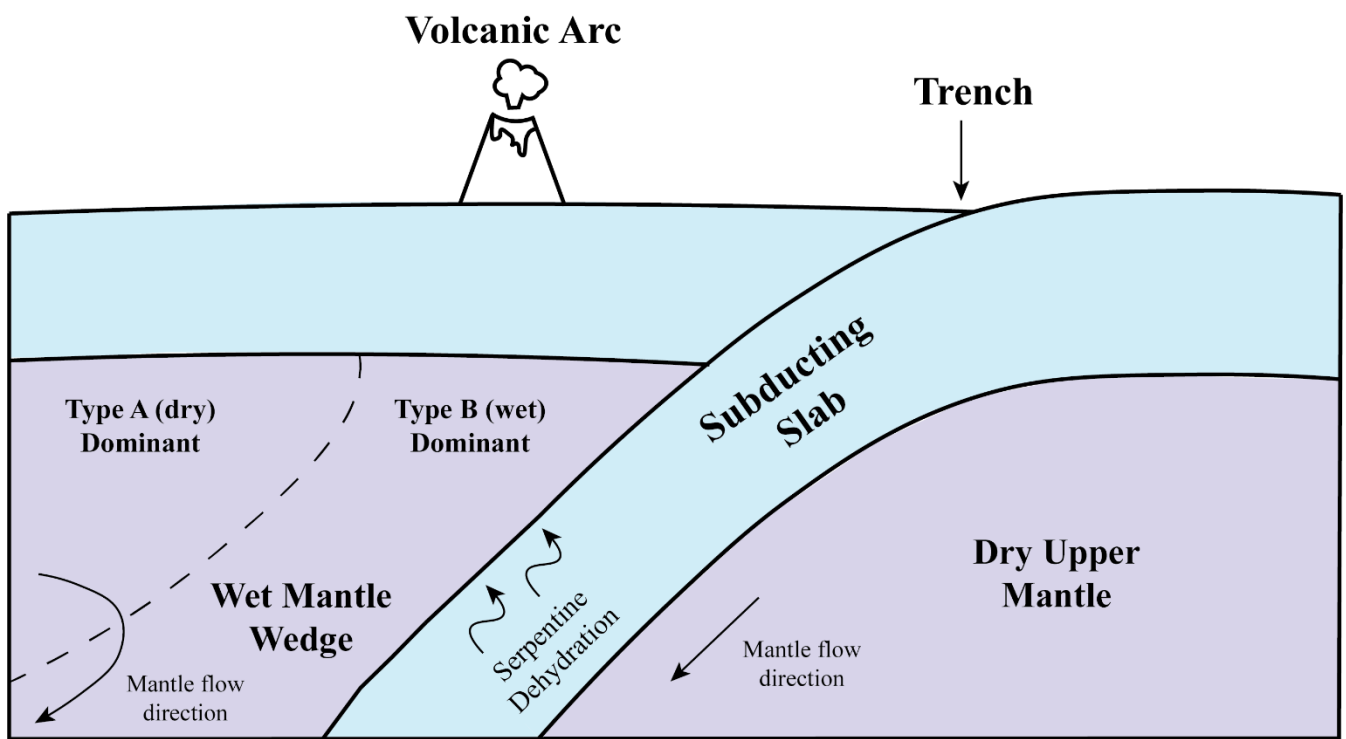


Figure 19. Illustration of a subduction zone showing regions of CPO dominance and transition as found by this study. Diagram not to scale.